Axis Dependent Conduction Polarity in the Air–Stable Semiconductor, PdSe$_2$

There exist a small number of compounds in which electrons and holes dominate transport simultaneously along different crystallographic directions. Most materials that exhibit this axis dependent conduction polarity are either metals, semiconductors with narrow band gaps less than 150 meV, or whose air sensitivity limits more detailed study and applications. The discovery of sizable band gap semiconductors with this phenomenon would enable their potential application in technologies that exploit the inherently efficient charge separation of thermally or optically excited carriers. Here we experimentally demonstrate that $PdSe_2$, an air-stable ~0.5 eV band gap semiconductor, exhibits this effect. We use $PdSe_2$ as a model material for establishing how the interplay between extrinsic doping concentrations and thermal activation of carriers controls the temperature above which axis dependent conduction polarity occurs. We show that lower concentrations of either p-type or n-type dopants triggers this phenomenon to emerge at lower onset temperatures. Overall, this work establishes $PdSe_2$ as the first technologically viable semiconductor with axis dependent conduction polarity, opening up new opportunities across a myriad of energy harvesting technologies.

COMMUNICATION

Axis Dependent Conduction Polarity in the Air-Stable Semiconductor, PdSe$_2$

Ryan A. Nelson, [a] Ziling Deng,[b] Andrew M. Ochs,[a] Karl G. Koster, [a] Cullen T. Irvine, [a] Joseph P. Heremans,[c,d] Wolfgang Windl[b] and Joshua E. Goldberger* [a]

Axis-dependent conduction polarity (ADCP) is a unique electronic phenomena in which the charge polarity of carrier conduction can differ from p-type to n-type depending on the direction of travel through the crystal. Most materials that exhibit ADCP are metals, and very few semiconducting materials exhibit this effect. Here, we establish that PdSe$_2$, a ~0.5 eV band gap semiconductor that is air- and water-stable exhibits ADCP, through the growth and characterization of the transport properties of crystals with extrinsic p- and n-type doping levels of Sb and Ir, respectively, in the 10^{16}-10^{18} cm^{-3}. Electron doped PdSe$_2$ exhibits p-type conduction in the cross-plane direction and n-type conduction along the in-plane directions above an onset temperature of 100-200 K that varies slightly with doping level. Lightly p-doped samples show p-type thermopower in all directions at low temperatures, but above ~360 K the in-plane thermopower turns negative. Density functional theory calculations indicate that the origin of ADCP arises from the complementary effective mass anisotropies in the valence and conduction bands in this material, which facilitate hole transport in the cross-plane direction, and electron transport along the in-plane directions. ADCP occurs at temperatures with sufficient thermal population of both carrier types to overcome the extrinsic doping levels to exploit the effective mass anisotropy. In total, the development of this stable semiconductor in which thermally or optically excited holes and electrons inherently migrate along different directions opens up numerous potential applications in a multitude of technologies.

1. Introduction

Almost all electronic materials typically exhibit a single majority carrier type, either electrons or holes, that dominates electronic transport uniformly along all directions of a crystal. In semiconductors, these n-type and p-type regions are then brought together to create virtually all modern functional electronic and energy conversion devices such as transistors, diodes, solar cells, and thermoelectrics. However, there is an emerging family of compounds that simultaneously exhibit either p-type or n-type majority conduction depending on the direction of travel through a single crystal[1-12], a phenomenon often referred to as axis-dependent conduction polarity (ADCP)[3, 4] or goniopolarity.[1, 2] Such materials promise to overcome inefficiencies in existing technologies by facilitating charge separation of electrons and holes. For instance, it has been recently shown that by exploiting the ADCP in Re$_4$Si$_7$, a new geometry of transverse thermoelectric modules can be fabricated that have efficiencies rivalling commercial longitudinal devices, but which do not suffer from the thermal degradation and efficiency losses caused by the hot side contacts. [9, 13-16]

Of the dozen or so materials in which axis dependent conduction polarity has been observed experimentally, only a small number of semiconductors with this effect have been discovered. This includes Re$_4$Si$_7$, which has a 0.15 eV band gap, CsBi$_4$Te$_6$, which has a 0.1 eV gap, NaSnAs, has a 0.64 eV gap, and finally the Mott insulator κ-(BEDT-TTF)$_2$Cu[N(CN)$_2$]Cl.[4, 8-10, 15, 17, 18] Although NaSnAs does have a sizeable band gap, its lack of air-stability, combined with the toxicity of As limits its potential applications. The development of semiconductors with appreciable band gaps that are also air and water stable, that can be easily grown in single crystal form, and with tunable doping levels, would enable the future exploration of this effect in light-activated applications such as photocatalysis and photovoltaics. In addition, such materials would enable a

[a.] Dept of Chemistry and Biochemistry, The Ohio State University, 100 W. 18th Ave. Columbus, OH 43210. E-mail: goldberger.4@osu.edu
[b.] Dept of Materials Science and Engineering, Fontana Laboratories Suite 2136, 140 W. 19th Ave., Columbus, OH 43210
[c.] Dept of Mechanical and Aerospace Engineering, The Ohio State University, 201 W. 19th Ave., Columbus, OH 43210
[d.] Dept of Physics, The Ohio State University, 191 W. Woodruff Ave., Columbus, OH 43210
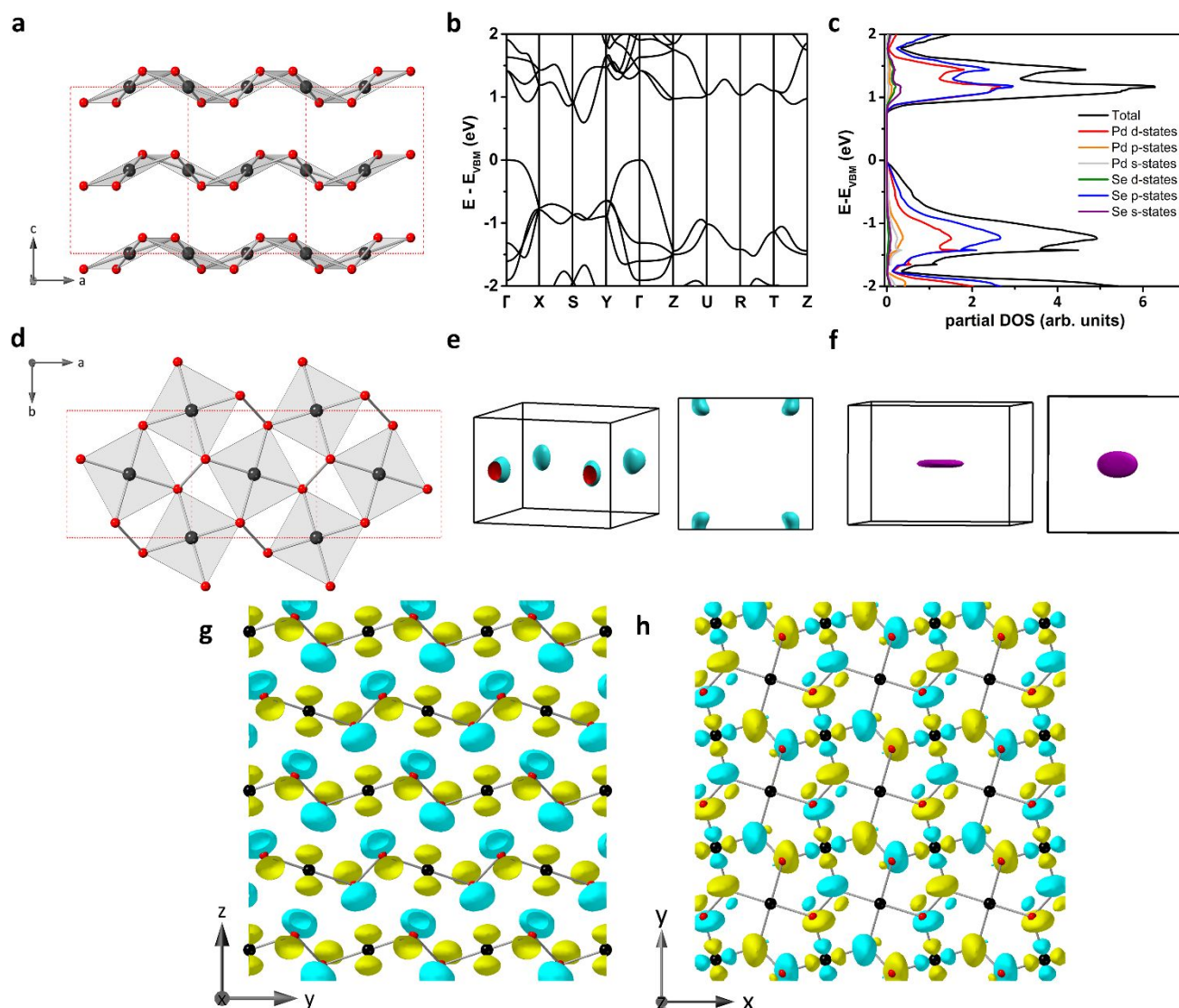
Figure 1. a) Crystal structure of orthorhombic $PdSe_2$, as viewed along the b-axis, showing the tilting of the $PdSe_4$ square planes. The black spheres correspond to Pd atoms and the red spheres correspond to Se atoms. **b)** DFT calculated band structure of orthorhombic $PdSe_2$. **c)** DFT calculated partial density of states for $PdSe_2$ showing the orbital character near the band extrema. **d)** Crystal structure of orthorhombic $PdSe_2$, as viewed along the c-axis, showing the diselenide dianion shared at the corner of four $PdSe_4$ square planes. **e)** DFT calculated Fermi surface near the conduction band minimum (CBM). Note the roughly prolate ellipsoidal shape of the surface, indicating anisotropic transport with lowest electron effective masses along the in-plane axes. **f)** DFT calculated Fermi surface near the valence band maximum (VBM), showing oblate ellipsoidal shape. **g)** Real component of the wavefunction of the VBM at the Γ point showing the cross-plane anti-bonding character of the mixed Pd $4d_z^2$ and Se $4p_z$ orbitals. **h)** Real component of the wavefunction of the lowest energy conduction band at S (near the CBM) showing the in-plane anti-bonding character of the mixed Pd $4d_{x^2-y^2}$ and Se $4p_x$ and $4p_y$ orbitals.

systematic understanding on the interplay between band structure, doping levels, and dopant activation energies on ADCP. Here, we show that $PdSe_2$, one member in a family of precious metal transition metal dichalcogenides that have attracted considerable recent interest[19-26], satisfies all these requirements and is an ideal model system for understanding the emergence of ADCP in semiconductors. Through the growth and characterization of the anisotropic transport properties of $PdSe_2$ single crystals with extrinsic p-type Ir and n-type Sb dopants in the range of 10^{16}-10^{18} cm^{-3} we show that this material exhibits ADCP at temperatures for which there is a sufficient concentration of both majority and minority carriers. A lower concentration of extrinsic dopants or sufficient counterdoping will shift the onset of ADCP to occur at lower temperatures. This furnishes the ability to control the onset of

ADCP, opening the door to tailoring systems for specific applications.

2. Results and Discussion

2.1 PdSe₂ Crystal and Band Structure

The orthorhombic $PdSe_2$ polymorph (which we hereafter refer to simply as $PdSe_2$) is a layered semiconductor that crystalizes in the *Pbca* space group (Fig 1a,b). Formally, the palladium can be considered cationic, Pd^{2+}, and the selenium forms a diselenide dianion, Se_2^{2-}. The layers are comprised of corner sharing $PdSe_4$ square planes which have a small tilt away from the c-axis mainly towards the a-axis. There are two layers per

unit cell. The Pd in one layer is almost on top of one of the Se atoms in the diselenide in the layer below. The crystal structure can be thought of as a derivative of the pyrite structure type but with a significant Jahn-Teller distortion of the Pd^{2+} d_{z}^2 orbitals, causing neighbouring layers to be held together mainly by van der Waals interactions.

The electronic structure and density of states were calculated by Density Functional Theory (DFT) using a hybrid functional approach.[27-31] The material is calculated to be a semiconductor with an indirect 0.58 eV band gap and a direct gap of about 1 eV. The indirect band lies between the Γ point in the valence band maximum (VBM) and a point between the S and Y points in the conduction band minimum (CBM), while the direct gap runs along a line approximately midway between the Γ and X points (Fig. 1c). The calculated band gap is within 100 meV of previously reported experimental values of the optical gap, which we also confirm subsequently with absorption measurements (section 2.2).[32] The partial DOS (Fig. 1d) indicate that the VBM and CBM are mostly mixed Pd 4d and Se 4p in character. The VBM at Γ is mainly composed of Pd $4d_{z}^2$ and Se $4p_z$ states in which the Pd $4d_{z}^2$ in one layer has a σ* antibonding configuration with the Se $4p_z$ orbitals in neighbouring layers (Fig. 1g). The CBM is dominated by σ* interactions between Pd $4d_{x}^2{}_{-y}^2$ and Se $4p_x$ and $4p_y$ states within each $PdSe_4$ square plane, but also has some partial Se $4p_z$ character (Fig. 1h). The Pd $4d_{z}^2$ character of the VBM and $4d_{x}^2{}_{-y}^2$ character of the CBM coincides with what one would expect the HOMO and LUMO to be for a d^8 square planar coordination compound, or a Jahn-Teller distorted octahedron. Because the VBM is predominantly comprised of orbitals that point along the c-axis, the VBM has a wide dispersion along the out of plane direction from Γ to Z and is relatively flat along the Γ to X and Γ to Y in-plane directions near the band edge. The valence band appreciably drops in energy on going from Γ to Z, because the interlayer Pd $4d_{z2}$/Se $4p_z$ σ* antibonding character become largely nonbonding, as shown in the wavefunction of the Z point (Fig. S1). This anisotropy in dispersion causes the Fermi surface near the VBM to have an oblate ellipsoidal shape (Fig. 1f). The strong $4d_z^2/4p_z$ orbital interactions in the VBM are also reflected in the calculated effective mass tensors (Table 1), in which the c-axis effective mass ($m_{zz,h}^*$) is -0.25 m_0, which is one and two orders of magnitude lighter than the b-axis ($m_{yy,h}$ = -3.9 m_0) and a-axis ($m_{xx,h}$ = -26.2 m_0) tensors, respectively. The CBM, which has a more prolate ellipsoidal shaped Fermi surface (Fig. 1e), has a-axis ($m_{xx,e}^*$) and b-axis ($m_{yy,e}^*$) effective masses of 0.24 m_0 and 0.26 m_0 which are about 2x lighter than the c-axis effective mass ($m_{zz,e}^*$), 0.46 m_0. The partial Se $4p_z$ character in this antibonding CBM reduces the degree of anisotropy compared to the valence band. Still, the strong directional preference for hole conduction along the cross-plane direction, combined with the opposite preference for electron conduction along the in-plane directions will lead to ADCP in $PdSe_2$.

2.2 $PdSe_2$ Crystal Growth and Optical Characterization

To empirically demonstrate that $PdSe_2$ hosts ADCP, large mm-scale crystals of $PdSe_2$ were synthesized using excess Se-flux either via slow cooling from the melt in a box furnace based off previous reports or using a vertical Bridgman method developed in-house (Fig. 2a,d).[33] Both methods yielded comparable crystal sizes and transport behaviour, although the Bridgman method had a much higher success rate for large single crystals. The crystal structure and phase purity were confirmed via powder x-ray diffraction (Fig. 2b). In addition, the different crystallographic axes were determined by the preferred orientation of diffraction peaks observed when different facets of the crystal are oriented towards the measurement plane, an example of the cross-plane orientation is shown in figure 2c, the strongly preferred 0 0 2 and 0 0 4 peaks can be clearly identified. Diffuse reflectance absorbance (DRA) measurements of $PdSe_2$ powders confirm the semiconducting behaviour (Fig. 2e,f). Reflectance data was converted to absorbance using the Kubelka-Munk equation. To deduce the direct and indirect optical gaps, the Tauc-Davis-Mott relations assuming a three-dimensional (3D) DOS, were applied to the absorbance data. The Tauc absorbance spectrum that assumes an allowed indirect transition shows an optical transition at 0.47 eV, while that which assumes an allowed direct mechanism shows an optical transition at about 0.72 eV (Fig. 2e,f). The small absorbance feature from ~0.82-0.91 eV is a measurement artifact attributed to a second harmonic of the O-H stretch of residual H_2O that is present in the $BaSO_4$ salt used as a diluent.

Table 1. Calculated electron and hole effective masses at the electron and hole pockets near the band extrema. Masses are reported as factors of m_0, the mass of a free electron.

	Effective Mass (m_0)	Effective Mass Tensor
Hole Pocket	-26.2	$m_{xx,h}^*$
	-3.9	$m_{yy,h}^*$
	-0.25	$m_{zz,h}^*$
Electron Pocket	0.24	$m_{xx,e}^*$
	0.26	$m_{yy,e}^*$
	0.46	$m_{zz,e}^*$

2.3 Doping Control

We will show in 2.4 that ADCP is observed when there is a sufficient concentration of both electron and hole carriers, which, requires higher temperatures for samples with higher extrinsic doping concentrations. However, at low temperatures, the sign of the thermopower remains the same along all the directions of the crystal, indicating a single carrier type dominates transport due to the presence of extrinsic p-type or n-type dopants. Initial syntheses yielded crystals that exhibited either p-type or n-type behaviour at low temperature. The presence and rough estimates of the concentration of extrinsic elements were then determined via Neutron Activation Analysis (NAA). All crystals analysed were estimated to have iridium concentrations in the range of 3-10 ppm (about $6 \cdot 10^{16} - 2 \cdot 10^{17}$ cm^{-3}), which was a reported impurity of the Pd source material. The n-type crystals were found to contain about 20 ppm Sb (about $7 \cdot 10^{17}$ $Sb \cdot cm^{-3}$). It is important to emphasize that the
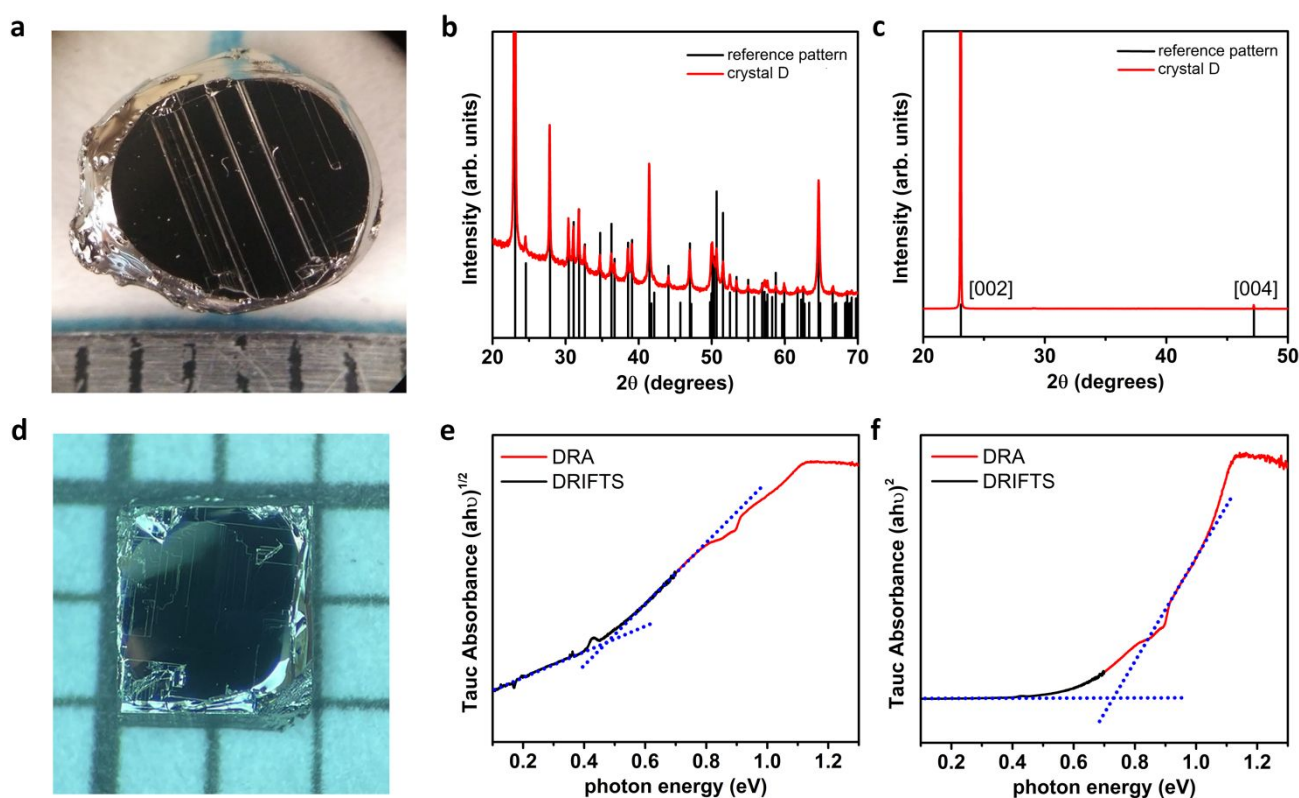
Figure 2. a) Image of an n-type PdSe$_2$ crystal (crystal D from main text) with a ruler for scale. The black lines on the bottom of the image mark one mm spacing. **b) Red:** Experimental powder X-ray diffraction pattern of PdSe$_2$ showing phase pure material. **Black:** Reference pattern for orthorhombic PdSe$_2$. **c) Red:** X-ray diffraction pattern oriented along the [00*l*] facet of crystal D. The prominent [002] and [004] peaks in the pattern show the expected preferred orientation along the cross-plane direction of a single crystal. **Black:** Expected peak positions from the reference pattern. **d)** Image of a p-type crystal after cleaving for use in a measurement device. The background grid is a one-mm grid. **e)** Tauc plot, assuming an allowed 3D indirect transition, showing the 0.47 eV optical band gap extracted by Kubelka-Munk treatment on a combined DRA and DRIFTS data set of PdSe$_2$. **f)** Tauc plot, assuming an allowed 3D direct transition, showing a 0.72 eV optical band gap extracted by Kubelka-Munk treatment on a combined DRA and DRIFTS data set of PdSe$_2$.

NAA measurements were qualitative in nature and designed for the identification of trace elements, therefore, the precise concentration of dopants are likely to be within an order of magnitude of these values. Still, the fact that Sb can act as an n-type dopant in PdSe$_2$ was confirmed by the intentional incorporation of roughly 10^{17} Sb·cm^{-3} during synthesis (crystal E in Fig. 4a). Iridium substitution onto the Pd site (Ir$_{Pd}$) is expected to lead to p-type doping assuming it remains divalent, as Ir^{2+} (d^7) would have one less electron than Pd^{2+} (d^8). Thus far, it is not well understood why Sb incorporation leads to n-type doping. Substituting Se for Sb (Se$_{Sb}$) is expected to result in p-type doping due to the removal of a valence electron. It is possible that with sufficiently an intercalation dopant rather than a substitutional dopant. Further work is necessary to more fully elucidate the chemical environment of antimony dopants in PdSe$_2$. Regardless of the exact nature of the dopant site, the ability to reliably achieve both p-type and n-type doping using different extrinsic dopants is demonstrated here and is of great technological importance for this emerging semiconductor.

2.4 Anisotropic Transport Measurements of p-doped Crystals

To characterize the anisotropic electronic transport in p-type PdSe$_2$, we employed standard cryostat measurements over a broad range of temperatures spanning from about 80 K to 560

K. The measurements were conducted on crystals that were wired into devices according to the general configuration shown in figure 3a and b. This measurement scheme allows for simultaneous thermal and electrical characterization.

Due to the Ir impurities in the PdSe$_2$ source material, hole conduction dominates the transport behaviour at lower temperatures. Here, the thermopowers sit near 700 µV·K^{-1} (Fig. 3c), reaching values as large as 1200 µV·K^{-1} for temperatures less than 100 K (Crystals A, B, C, Fig. S2). The in-plane and cross-plane thermopowers both decrease sharply with temperature above 300 K (Fig. 3c). While the cross-plane thermopower plateaus with increasing temperature near 200 µV·K^{-1}, the in-plane thermopower continues dropping, crossing to negative values near 360 K, confirming ADCP. The in-plane thermopower plateaus near -300 µV·K^{-1} (Fig. 3c) at temperatures >450 K. Again, based off the calculated effective masses, we expect hole conduction to dominate cross-plane transport and electron-conduction to dominate in-plane transport. This is reflected in the signs of the thermopowers at high temperatures. In total, the magnitude of the in-plane thermopowers and the crossover temperatures are relatively consistent across several crystals with similar doping concentrations (Fig. S2a)

There is a decrease in resistivity with increasing temperature, expected for a non-degenerately doped p-doped semiconductor. The resistivities range from 10^0 to 10^{-2} Ω·m
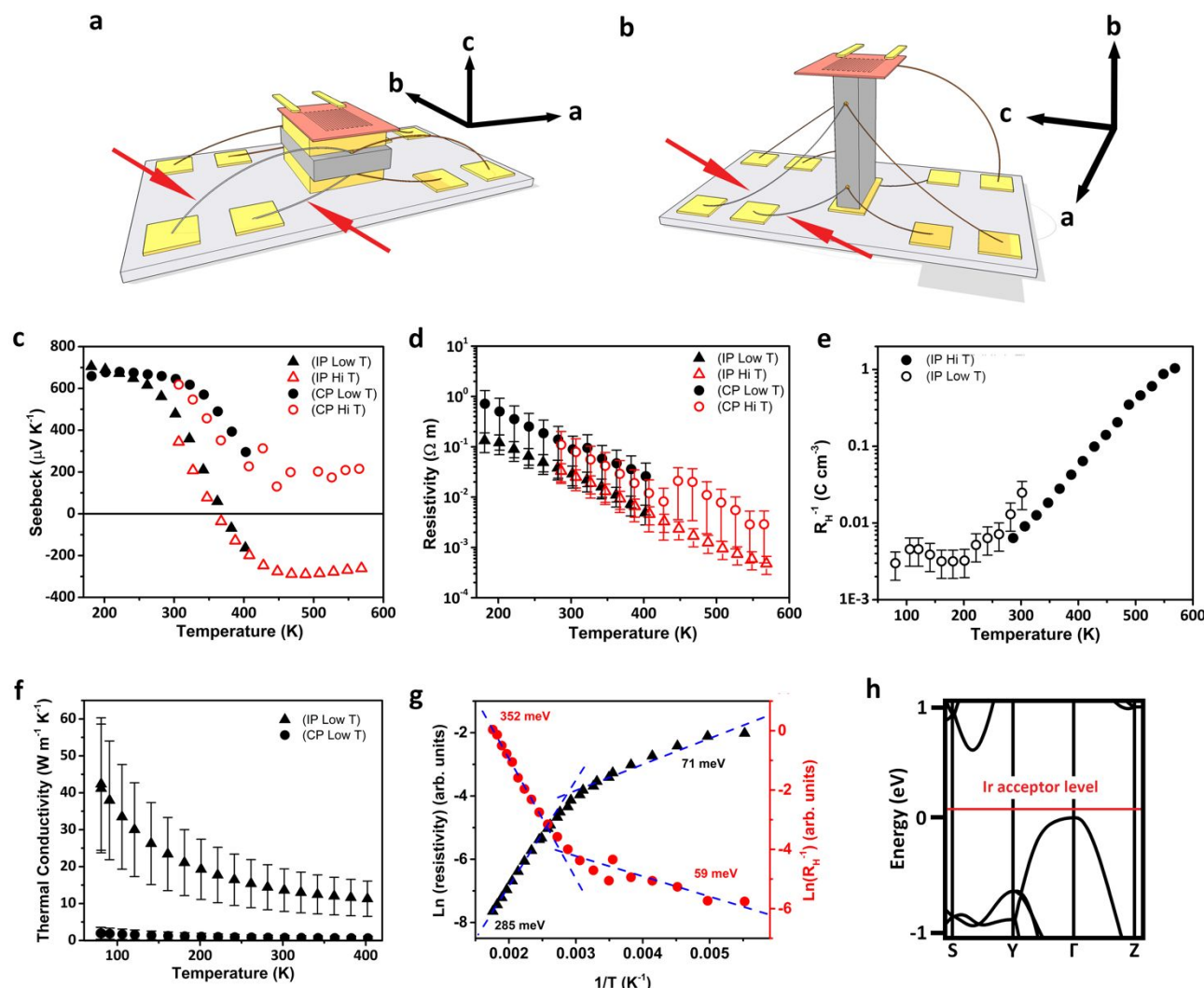
Figure 3. a) Schematic illustration of a typical cross-plane measurements device. The base plate is a wafer of alumina. The yellow contacts signify brass or copper current spreaders and heat sinks. The block in the middle of the schematic is the crystal in the appropriate geometry for measurement. The salmon-coloured plate is a resistive heating unit which furnishes the thermal gradient for the thermal measurements. The wires contacting the device and baseplate are all copper except for those denoted by the red arrows, these are constantan wires for the thermocouples. **b)** Schematic illustration of a typical in-plane measurement device. All elements of the schematic are the same as previously described for the cross-plane device **c)** Measured in-plane and cross-plane thermopowers for p-type $PdSe_2$. **d)** Measured in-plane and cross-plane resistivities for p-type $PdSe_2$. **e)** Measured in-plane inverse Hall coefficient. **f)** Thermal conductivity measurements on p-type $PdSe_2$. **g)** Arrhenius treatment of the lightly doped p-type $PdSe_2$ showing that in the lower temperature regime the acceptor states have an activation energy of 59-71 meV, but the high temperature regime shows intrinsic behaviour with the activation barrier corresponding to roughly half the band gap. **c-g)** were all measured on the same crystal, crystal A. **h)** Approximate location of the chemical potential of Ir acceptor states in $PdSe_2$.

along the cross-plane direction and about 3×10^{-1} to 5×10^{-3} Ω·m along the in-plane direction (Fig. 3d). The resistivities of multiple lightly doped crystals are quite close and within a factor of three (Fig. S2b). Next, in-plane Hall effect measurements were collected on this lightly doped crystal (crystal A) (Fig. 3e). The Hall coefficients were positive across all temperatures. A rigorous analysis of the anisotropic mobilities and electron and hole concentrations is complicated by the two-carrier nature of this moderate gap semiconductor. However, at low temperatures the transport properties should be dominated by extrinsic dopants. Thus, we decided to estimate dopant levels using the single carrier approximation and the low temperature values to make comparisons between crystals. For Crystal A, from 100-200 K, the hole density was estimated to range from $2-3 \times 10^{16}$ cm^{-3}, which is well within the uncertainties expected from the NAA measurements. In addition, the 200 K Hall

mobility using this single carrier model is estimated to be 30 cm^2 V^{-1} s^{-1}.

The thermal conductivity measurements give a decrease in thermal conductivity with temperature. This is expected for semiconductor materials for which lattice thermal conduction dominates. The in-plane thermal conductivity ranges from about 40 W·m^{-1}·K^{-1} at 80 K to about 15 W·m^{-1}·K^{-1} at 400 K (Fig. 3f). The cross-plane thermal conductivity is significantly supressed relative to the in-plane values as expected for a van der Waals material. Here, the 80 K cross-plane thermal conductivity is less than 3 W·m^{-1}·K^{-1} and drops to around 0.5 W·m^{-1}·K^{-1} at 400 K (Fig. 3f). The in-plane thermal conductivities of several lightly-doped crystals are all within the measurement uncertainties of each other (Fig S2c).

Next, we evaluated the temperature dependence of the carrier concentration and resistivity using an Arrhenius treatment to determine the activation energies of the different
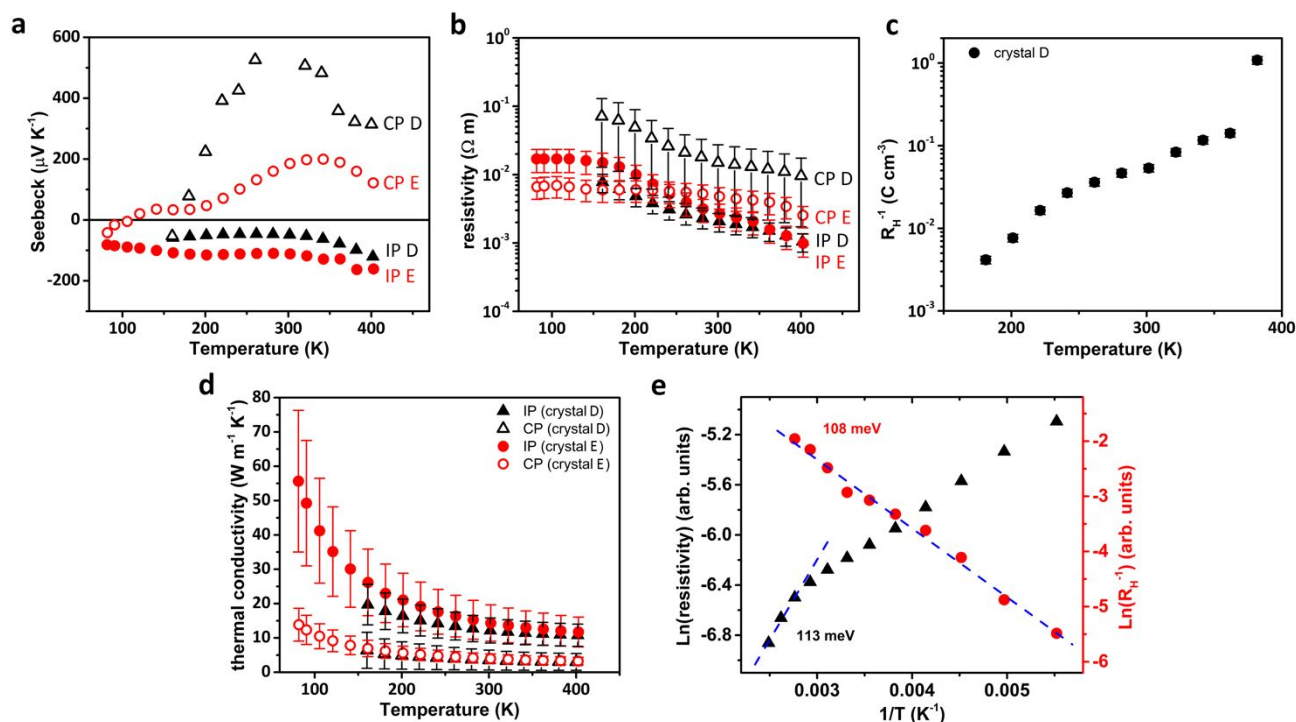
Figure 4. a) Measured in-plane and cross-plane thermopowers for 2 different n-type PdSe$_2$ crystals. **b)** Measured in-plane and cross-plane resistivities for the n-type samples. **c)** Measured in-plane inverse Hall coefficient on Crystal D. **d)** Thermal conductivity measurements on the n-type samples. **e)** Arrhenius treatment on crystal D showing the activation energy following Sb doping. Slopes extracted via equations 1 and 2 from the main text (section 2.4).

transport regimes. The Arrhenius treatment is based on the formulae (1) and (2), which assume diffusive transport,

$$\ln\ (\rho_T) = \ln\ (\rho_0) + \frac{E_A}{k_B T} \qquad (1)$$

$$\ln\ (R_{H,T}{}^{-1}) = \ln\ (R_{H,0}{}^{-1}) - \frac{E_A}{k_B T} \qquad (2)$$

Where ρ_T is the resistivity at temperature T, ρ_0 is a pre-exponential resistivity factor, $R_{H,T}{}^{-1}$ is the inverse Hall coefficient at temperature T and is proportional to the carrier density, $R_{H,0}{}^{-1}$ is a pre-exponential inverse Hall coefficient factor, E_A is the activation energy, k_B is Boltzmann's constant, and T is the temperature in K. The Arrhenius treatments were performed using the in-plane transport data, since the cross-plane transport measurements have much higher uncertainties and noise due to the inherently thin c-axis crystal dimensions. When the natural logarithm of resistivity or inverse Hall coefficient is plotted as a function of inverse temperature, the slope is the activation energy divided by Boltzmann's constant. This treatment allows for extraction of the activation energy of the thermally activated carriers and gives an approximate position of the acceptors or donors relative to the band extrema.

Figure 3g shows an Arrhenius treatment of the resistivity and carrier densities, which both give similar values for the activation energies of carriers. This treatment covers two regimes, the lower temperature regime (180 to 300 K), and the high temperature regime (400 to 560 K). These two temperature windows give different slopes and activation barriers, indicative of two different thermal excitation regimes. The transition between the two different activation energy

regimes in these in-plane is very similar to the temperature at which the in-plane thermopower changes sign. The lower temperature regime is calculated to have a $59 - 71$ meV activation energy. Here, because the lower temperature thermopowers are positive, it can be assumed that the system is p-doped, thus we attribute this activation energy to the position of Ir acceptor levels above the VBM. At higher temperatures, an activation energy of 285 to 350 meV is observed. This corresponds to half the band gap, and thus indicative of thermal excitation of carriers across the band gap.

PdSe$_2$ with higher Ir concentrations of ~5 x 10^{17} cm^{-3} were synthesized (Crystals F, G, H - Fig. S3). The in-plane thermopowers of these crystals are positive across all measured temperatures and do not turn negative, even up to 400 K (Fig S3a). The observed thermopowers sit near 600 μV·K^{-1} (Fig. 3c), reaching values as large as 900 μV·K^{-1} for temperatures less than 100 K. These values are smaller than the more lightly Ir-doped crystals. This suppressed thermopower would be expected with greater doping. The in-plane resistivities range from 5 x 10^{-2} to 1 x 10^{-3} Ω·m which is lower than in the lightly doped crystals (Fig. S3b), again, as would be expected. The Hall coefficients again were positive across all temperatures, and using a single carrier approximation, from 100-200K ranged from 1-5 x 10^{17} cm^{-3} (Fig. S3c). The in-plane thermal conductivity of these more heavily doped samples ranged from about 28-32 W·m^{-1}·K^{-1} at 80 K to about 12-15 W·m^{-1}·K^{-1} at 400 K (Fig. S3d). These values are essential identical to lightly doped samples, within variance, indicating that even at this higher doping level the lattice component dominates the thermal conductivity. The Arrhenius treatment of the carrier concentration and the resistivity show an activation energy of 61-68 meV. (Fig. S3e) This is essentially

identical to the more lightly doped samples further suggesting that this barrier reflects the activation energy of the Ir acceptor level above the valence band maximum (Fig. S3f). In these heavily doped samples, the intrinsic activation energy of $E_g/2$ is not observed in the Arrhenius plot up to 400 K in contrast to the more lightly p-doped crystals. This is expected, since the greater extrinsic doping level requires a higher density of thermally activated carriers to reach the intrinsic regime.

Together, this data shows that the temperature range in which ADCP in PdSe$_2$ is observed for the p-type samples is highly dependent on the extrinsic doping level. When the chemical potential is far from the intrinsic level, carriers will require greater thermal energy for the electrons to populate the CBM, and holes to populate the VBM. Sufficient quantities of both electron and hole carriers is essential to observe ADCP. In other words, when one carrier type is in excess over the other by a critical amount, the thermopower along all dimensions will be dominated by the excess carriers over a large temperature range.

2.5 Anisotropic Transport Measurements of n-doped Crystals

Despite the presence of Ir in our Pd source, we discovered that with sufficient quantities of Sb counter doping (10^{16-17}), n-type behaviour could be observed (Crystals D, E, Fig. 4). In both crystals, both the cross-plane and in-plane thermopower start negative at low temperature (<180 K). But, as temperature increases so do the cross-plane thermopowers, ultimately peaking around 550 µV·K^{-1} and 200 µV·K^{-1} for crystal D and E, respectively. Both crystals gave very similar in-plane thermopowers that remained negative over the entire temperature range, dropping to about -150 µV·K^{-1} at 400 K (Fig 4a). The differences in CP thermopowers are likely due to small differences in the antimony concentrations.

Electronic transport measurements on these n-type crystals show decreasing resistivity with increasing temperature, again, expected for non-degenerately doped semiconductors. The resistivities ranged from 7 x 10^{-2} to 10^{-3} Ω·m from 100 to 400 K (Fig. 4b). The differences in resistivity values between the two samples for the in-plane and cross-plane directions are within the variance, although small differences between the two samples are likely to reflect different doping concentrations. The 200K in-plane Hall effect measurements on Crystal D (Fig. 4c) reflect an electron doping level of 2-5 x 10^{16} cm^{-3} and a Hall mobility of 270 cm^2 V^{-1} s^{-1} using a single carrier approximation. This is indicative of a greater quantity of Sb than the native Ir impurity concentration introduced by the Pd source material.

Thermal conductivity measurements show the expected T^{-1} trend indicating Umklapp scattering in a lattice dominated structure (Fig. 4d). The low temperature values peak at about 55 W·m^{-1}·K^{-1} for the in-plane direction and 15 W·m^{-1}·K^{-1} in the cross-plane direction. The 400 K values, on the other hand, drop to about 15 W·m^{-1}·K^{-1} and 5 W·m^{-1}·K^{-1} for in-plane and cross-plane, respectively. These values are within the variance of the p-type samples.

The Arrhenius treatment for the n-type crystals is given in figure 4e and, again uses equations 1 and 2, to determine an activation energy of 108 – 113 meV. The fact that there are both Sb and Ir counterdopants complicates the exact assignment of the activation energy. One interpretation is that the activation energy extracted from the resistivity and Hall data could approximate the energy level of the Sb donor states relative to the CBM. While this activation energy might be related to the donor activation energy, it might also correspond to a polaronic or impurity band hopping activation energy. Regardless of the mechanism, the presence of Sb clearly results in n-type doping in PdSe$_2$.

3. Conclusions

We have shown that PdSe$_2$ is a semiconductor, with an indirect band gap of about 0.5 eV, that exhibits ADCP. Furthermore, we have established how to extrinsically dope this semiconductor both p-type and n-type using iridium and antimony, respectively. We show that the extrinsic doping level can control the onset of ADCP. Overall, this work indicates that there is a critical window of extrinsic doping concentrations, wherein simultaneous positive and negative thermopowers along orthogonal directions occurs. The size of this window is expected to depend on the band gap and effective mass anisotropies of both the conduction and valence bands. The ability to access ADCP in semiconductor materials is expected to be highly beneficial for applications that rely on carrier separation for functionality, such as thermoelectrics, solar cells, or optoelectronics.

4. Experimental

Crystal Growth Methods

Crystals of PdSe$_2$ were grown by two different methods. The first method is a simple self-flux with a 4-molar excess of selenium (molar ratio of 1:6 Pd:Se). Taking care not to overload the fused-silica ampoule with volatile selenium, a typical 850-mg charge of elemental Pd (99.95% Alfa Aesar) and Se (99.999% Alfa Aesar) powder is ground and added to the ampoule. The ampoule is then evacuated to typical vacuum pressures of around 60 mtorr (8 x 10^{-5} atm) and flame sealed. The ampoule is then heated to 850°C over the course of twelve hours and held at 850°C for 50 hours. Crystallization occurs upon slowly cooling to 450°C in 400 hours. The ampoule is finally allowed to cool with the furnace from 450°C to room temperature. After the growth, the product ingot is extracted from the selenium flux by melting it off under a thermal gradient at 500°C. Single crystals grown by this method typically have in-plane dimensions on the order of 5 mm and cross plane thicknesses of <0.5 mm.

The second method is a Bridgman type growth from the melt. Elemental Pd powder is mixed with a large excess of elemental Se powder (molar ratio of 3:97 Pd:Se). The typical 7-gram charge is loaded into a fused-silica ampoule with 2-3 mm thick walls and a tapered end. It is important to ensure that

even if all of the Se was volatilized, the pressure generated would be much less than the critical hoop stress of fused silica (< 50 MPa). The ampoule is evacuated and sealed under a typical vacuum pressure of around 60 mTorr (8 x 10^{-5} atm). After sealing, a small fused-silica hook is welded to the ampoule opposite the tapered end. The ampoule is then suspended by this hook within a vertical single-zone tube furnace using nichrome wire to suspend the ampoule. To grow the $PdSe_2$ single crystals, the ampoule is suspended in the vertical furnace which is ramped up to 850°C in 24 hours. The temperature is held at 850°C for 50 hours before the ampoule is dropped through the natural thermal gradient of the vertical furnace at a rate of 1 mm hr^{-1} over the course of ~100 h. The temperature is then dropped to room temperature over twelve hours. Single crystals grown by this method typically have in-plane dimensions on the order of 3 − 6 mm and cross plane thicknesses of <1 mm.

Doped crystals were grown using growth method 2 by introducing the appropriate quantity of dopant element to the reagent mixture before synthesis. To achieve the 10^{16} to 10^{18} cm^{-3} concentrations of dopants a solid-state serial dilution was performed. An initial concentration of the dopant was mixed into a known quantity of Se. The dopant concentration was then reduced by diluting a portion of the previous mixture in fresh Se. This dilution process was carried out several times before the final concentration was reached. Thorough grinding between each dilution was crucial for maintaining mixture homogeneity.

Optical measurements

Optical characterization was performed using a PerkinElmer Frontier dual-range IR spectrometer for the low energy range of the Kubelka-Munk absorption plots. The high energy range was collected via a PerkinElmer Lambda 950 UV/vis spectrophotometer with an integrating sphere. Data was collected on the IR instrument in diffuse reflectance infrared Fourier transform spectroscopy mode (DRIFTS) while the data from the UV-Vis instrument was collected under diffuse reflectance absorption mode (DRA).

Transport measurements

Thermoelectric transport properties were measured using a standard liquid N_2 cryostat at temperatures ranging from 80 to 400 K, and in a high temperature cryostat from 300 − 560 K. A small brass sheet was attached to the top of the crystal underneath a resistance heater, and an alumina sheet acted as a heat sink, to ensure uniform heat flow. Copper–constantan thermocouples were attached at two points along the crystal with Ag or Au epoxy to measure the temperature gradient, and the copper legs of the thermocouples were also used to measure the Seebeck voltage. Thermal conductivity measurements were collected along the in-plane direction using the classical heater-and-sink method. Here, the amount of heater power divided by the temperature drop across the sample gives the thermal conductance, which is subsequently converted to conductivity using the sample dimensions. For the

collection of 4-probe resistivity measurements, copper current wires were attached to the top and bottom of the crystals. For Hall coefficient measurements along the in-plane direction, an additional set of copper wires were attached in a direction transverse to both heat flow and the applied magnetic field. The magnetic field was varied from −1.9 T to +1.9 T. The stated carrier densities and Hall mobilities were estimated using a single carrier-type approximation. Thermopower and resistivity measurements were first performed in the in-plane orientation, and then, contacts were removed and reattached in the cross-plane orientation, allowing for measurements in both directions to be collected on the same single crystals.

Calculations

The DFT calculations were performed on a $PdSe_2$ primitive cell within the Vienna Ab initio Simulation Package using Perdew-Burke-Ernzerhof implemented in the meta-GGA SCAN functional together with van der Waals corrected functionals.[27-31] The relaxed configuration was obtained using a 4x4x4 k-point grid and a plane-wave energy cutoff of 400 eV.

Conflicts of interest

There are no conflicts to declare.

Acknowledgements

Notes and references

1. B. He, Y. X. Wang, M. Q. Arguilla, N. D. Cultrara, M. R. Scudder, J. E. Goldberger, W. Windl and J. P. Heremans, *Nat. Mater.*, 2019, **18**, 568-572
2. Y. X. Wang and P. Narang, *Phys. Rev. B: Condens. Matter Mater. Phys.*, 2020, **102**, 125122
3. Y. X. Wang, K. G. Koster, A. M. Ochs, M. R. Scudder, J. P. Heremans, W. Windl and J. E. Goldberger, *J. Am. Chem. Soc.*, 2020, **142**, 2812-2822
4. A. M. Ochs, P. Gorai, Y. X. Wang, M. R. Scudder, K. Koster, C. E. Moore, V. Stevanovic, J. P. Heremans, W. Windl, E. S. Toberer and J. E. Goldberger, *Chem. Mater.*, 2021, **33**, 946-951
5. V. A. Rowe and P. A. Schroeder, *J. Phys. Chem. Solids*, 1970, **31**, 1-8
6. A. Burkov and M. Vedernikov, *Fiz. Tverd. Tela*, 1986, **28**, 3737-3739

7. A. T. Burkov, M. V. Vedernikov, V. A. Elenskii and G. P. Kovtun, *Fiz. Tverd. Tela*, 1986, **28**, 785-788

8. Y. Kawasugi, K. Seki, Y. Edagawa, Y. Sato, J. Pu, T. Takenobu, S. Yunoki, H. M. Yamamoto and R. Kato, *Appl. Phys. Lett.*, 2016, **109**, 233301

9. M. R. Scudder, K. G. Koster, J. P. Heremans and J. E. Goldberger, *Appl. Phys. Rev.*, 2022, **9**, 021420

10. D. Y. Chung, T. P. Hogan, M. Rocci-Lane, P. Brazis, J. R. Ireland, C. R. Kannewurf, M. Bastea, C. Uher and M. G. Kanatzidis, *J. Am. Chem. Soc.*, 2004, **126**, 6414-6428

11. W. Kiehl, H. Duan and A. Hermann, *Phys. C (Amsterdam, Neth.)*, 1995, **253**, 271-278

12. J. Dolinšek, M. Komelj, P. Jeglič, S. Vrtnik, D. Stanić, P. Popčević, J. Ivkov, A. Smontara, Z. Jagličić and P. Gille, *Phys. Rev. B: Condens. Matter Mater. Phys.*, 2009, **79**, 184201

13. Y. Tang, B. Y. Cui, C. L. Zhou and M. Grayson, *J. Electron. Mater.*, 2015, **44**, 2095-2104

14. C. Zhou, S. Birner, Y. Tang, K. Heinselman and M. Grayson, *Phys. Rev. Lett.*, 2013, **110**, 227701

15. M. R. Scudder, B. He, Y. Wang, A. Rai, D. G. Cahill, W. Windl, J. P. Heremans and J. E. Goldberger, *Energy Environ. Sci.*, 2021, **14**, 4009-4017

16. S. Harada, K. Tanaka, K. Kishida and H. Inui, *Adv. Mater. Res.*, 2007, **26**, 197-200

17. N. Nakamura, Y. Goto and Y. Mizuguchi, *Appl. Phys. Lett.*, 2021, **118**, 153903

18. M. Omprakash, H. Usui, K. Yanagi, Y. Mizuguchi and Y. Goto, *Mater. Today Commun.*, 2022, **31**, 103558

19. L.-S. Lu, G.-H. Chen, H.-Y. Cheng, C.-P. Chuu, K.-C. Lu, C.-H. Chen, M.-Y. Lu, T.-H. Chuang, D.-H. Wei and W.-C. Chueh, *ACS Nano*, 2020, **14**, 4963-4972

20. L. Pi, C. Hu, W. Shen, L. Li, P. Luo, X. Hu, P. Chen, D. Li, Z. Li and X. Zhou, *Adv. Funct. Mater.*, 2021, **31**, 2006774

21. M. Fu, L. Liang, Q. Zou, G. D. Nguyen, K. Xiao, A.-P. Li, J. Kang, Z. Wu and Z. Gai, *J. Phys. Chem. Lett.*, 2019, **11**, 740-746

22. M. Li, W. Luo, X. Zhang, M. Zhu, G. Peng, Z. Zhu and S. Qin, *ACS Appl. Electron. Mater.*, 2023,

23. Y. Zhao, P. Yu, G. Zhang, M. Sun, D. Chi, K. Hippalgaonkar, J. T. Thong and J. Wu, *Adv. Funct. Mater.*, 2020, **30**, 2004896

24. J. H. Ryu, K. H. Lee, S.-w. Hong, J. Y. Hwang, Y. Yi, S. Im, S.-i. Kim, S. Y. Kim and K. Lee, *Scr. Mater.*, 2020, **182**, 6-10

25. I. Pallecchi, N. Manca, B. Patil, L. Pellegrino and D. Marré, *Nano Futures*, 2020, **4**, 032008

26. W. Y. Lee, M. S. Kang, J. W. Choi, S. H. Kim, N. W. Park, G. S. Kim, Y. H. Kim, E. Saitoh, Y. G. Yoon and S. K. Lee, *Adv. Sci.*, 2022, **9**, 2203455

27. G. Kresse and J. Furthmüller, *Phys. Rev. B: Condens. Matter Mater. Phys.*, 1996, **54**, 11169

28. P. E. Blöchl, *Phys. Rev. B: Condens. Matter Mater. Phys.*, 1994, **50**, 17953

29. J. Sun, A. Ruzsinszky and J. P. Perdew, *Phys. Rev. Lett.*, 2015, **115**, 036402

30. A. Tkatchenko, R. A. DiStasio Jr, R. Car and M. Scheffler, *Phys. Rev. Lett.*, 2012, **108**, 236402

31. S. Grimme, *J. Comput. Chem.*, 2006, **27**, 1787-1799

32. G. Zhang, M. Amani, A. Chaturvedi, C. Tan, J. Bullock, X. Song, H. Kim, D.-H. Lien, M. C. Scott and H. Zhang, *Appl. Phys. Lett.*, 2019, **114**, 253102

33. A. D. Oyedele, S. Z. Yang, L. B. Liang, A. A. Puretzky, K. Wang, J. J. Zheng, P. Yu, P. R. Pudasaini, A. W. Ghosh, Z. Liu, C. M. Rouleau, B. G. Sumpter, M. F. Chisholm, W. Zhou, P. D. Rack, D. B. Geohegan and K. Xiao, *J. Am. Chem. Soc.*, 2017, **139**, 14090-14097